Room Temperature Ferroelastic Creep Behavior of Porous $(La_{0.6}Sr_{0.4})_{0.95}Co_{0.2}Fe_{0.8}O_{3-\delta}$

Barbara Arnauda [1], Ali Akbari-Fakhrabadi [1,*], Nina Orlovskaya [2], Viviana Meruane [3] and Wakako Araki [4]

[1] Advanced Materials Laboratory (AmLab), Department of Mechanical Engineering, University of Chile, Santiago 8370456, Chile; barbara.arnauda@ug.uchile.cl

[2] Department of Mechanical and Aerospace Engineering, University of Central Florida, Orlando, FL 32816, USA; Nina.Orlovskaya@ucf.edu

[3] Laboratory of Mechanical Vibrations and Rotodynamics (LMVR), Department of Mechanical Engineering, University of Chile, Santiago 8370456, Chile; vmeruane@uchile.cl

[4] Department of Mechanical Engineering, Saitama University, 255 Shimo-okubo, Sakura-ku, Saitama 338-8570, Japan; araki@mech.saitama-u.ac.jp

*   Correspondence: aliakbarif@uchile.cl

Abstract: The time-dependent deformation of porous $(La_{0.6}Sr_{0.4})_{0.95}Co_{0.2}Fe_{0.8}O_{3-\delta}$ (LSCF) under constant uniaxial compressive stress at room temperature has been studied. Both axial and lateral stress–strain deformation curves clearly show the non-linear ferroelastic behavior of LSCF perovskite during compression. The ferroelastic characteristics of deformation curves such as coercive stress and apparent loading moduli decrease when the porosity of the samples increases. Ferroelastic creep deformations at applied stresses of 25 and 50 MPa demonstrate that stress and porosity are influencing factors on creep deformation, which increases with increasing stress and porosity. A negative creep or axial expansion and lateral contraction were observed in the sample with 35% porosity under 50-MPa constant compression stress.

Keywords: ferroelasticity; creep; LSCF; porosity

1. Introduction

Ternary oxide ceramics with ABO_3 perovskite structures attract the scientific community due to their unique properties which depend on a number of different parameters such as a possibility of modifying their compositions by doping both on the A- and B-site of cations sub-lattice of the perovskites [1]. One of the interesting classes of perovskite materials is mixed ionic- and electronic-conducting $LaCoO_3$-based perovskites, which are outstanding materials broadly used in solid oxide cells as oxygen electrodes for efficient energy conversion when they are doped by Sr on the A-site and Fe on the B-site of the cation sub-lattice [2,3]. It is generally accepted that most polycrystalline $LaCoO_3$-based perovskites possess a cubic symmetry during high-temperature processing and this cubic structure transforms to low symmetry phases such as rhombohedral upon cooling [4]. The low symmetry of the transformed phase leads to the formation of twins in alternating patterns to release stresses related with transformation strains [5,6]. The non-linear behavior along with hysteresis in the stress–strain curve of materials with reduced symmetry below Curie temperature when external forces are applied is known as ferroelastic behavior [7–9]. The behavior has been mostly characterized by uniaxial compression using the stress–strain curves in the first loading–unloading cycle and by detecting a critical stress for the initiation of domains switching (σ_c) and switching strain ($\Delta\varepsilon_s$) determined by the intersection of initial (E_1), switching (E_s), and loading tangent moduli (E_2) [10,11].

Room temperature time-dependent deformation is one of the characteristic features of ferroelastic perovskites, which occurs because of the mobility of domain (twin) walls in the microstructure and their interactions with lattice defects such as oxygen vacancies and grain boundaries to name a few [12]. The ferroelastic time-dependent deformation has been reported in ferroelectric lead zirconate titanate [13,14] and ferroelastic lanthanum cobaltite-based perovskites [3,11,15–17]. Unlike high-temperature creep which usually reaches a steady-state strain rate under a constant stress, ferroelastic time-dependent deformation exhibits a continuous decreasing creep rate [3,11,16,17] or an unusual expansion of the sample under a constant compressive stress called negative creep which has been reported for $LaCoO_3$ [12] for the first time. The ferroelastic creep mechanisms are different from those occurring in materials at high temperatures [11,14]. Lugovy et al. [16] experimentally investigated room-temperature creep at different stresses in polycrystalline $LaCoO_3$-based oxides under compression stress and found ferroelastic domain switching as a mechanism for ferroelastic creep and proposed a phenomenological model of the ferroelastic creep. However, their work was based on creep deformation during short periods of 180 s. Araki and Malzbender [3], who studied ferroelastic creep deformation of $(La_{0.6}Sr_{0.4})_{0.95}Co_{0.2}Fe_{0.8}O_{3-\delta}$ (LSCF), suggested a Prony series-type equation. The research performed on ferroelastic room temperature creep of $LaCoO_3$-based perovskites is rather limited to only a small number of published papers and therefore, in the present study, the room temperature ferroelastic time-dependent deformation of porous $(La_{0.6}Sr_{0.4})_{0.95}Co_{0.2}Fe_{0.8}O_{3-\delta}$ (LSCF) has been reported using a digital image correlation technique which was found to be a useful method to measure axial and lateral strain–stress curves and creep deformations.

2. Experimental

To prepare perovskite samples for compression experiments with different amount of porosity, commercial $(La_{0.6}Sr_{0.4})_{0.95}Co_{0.2}Fe_{0.8}O_{3-\delta}$ (LSCF-HP, Fuel Cell Materials, Lewis Center, OH) powder was mixed with 5 and 20 wt % polymethyl methacrylate (PMMA-MX-500, Soken Chemical and Engineering, Tokyo, Japan) powder as pore-former by planetary ball milling for 6 h. Based on the amount of added PMMA pore-former (5 and 20 wt %), the samples were named LSCF-P5 and LSCF-P20, respectively. To fabricate rectangular bars, the milled powders were uniaxially pressed (90 MPa), and were subsequently sintered at 1200 °C for 3 h with heating and cooling rates of 60 and 30 °C/h, respectively. The sintered bars were grinded, polished to final dimensions of 8 × 4 × 4 mm and annealed at 1100 °C for one hour with the same heating and cooling rates used for sintering to remove residual strain due to ferroelastic domain switching [3]. The bulk density of samples was measured by a geometrical method and scanning electron microscopy (SEM) micrographs of annealed surfaces and fracture surfaces of samples were used for grain and pore size measurements, respectively.

The prepared bars were placed on an alumina disc (diameter = 20 mm, thickness = 10 mm) with one zirconia semisphere (diameter = 10 mm) on the top for loading. The load was raised from 0.4 MPa preloading stress to the maximum stress of 25 and 50 MPa with a 5-kN load cell (Xforce HP), held for 3 h and unloaded to 0.4 MPa. The loading and unloading rates were maintained at 120 N/min for all tests. A digital image correlation technique (DIC) which has the advantages of accuracy and low requirements of vibration isolation [18], especially for creep deformation for long-time tests, were implemented in this study for deformation measurements by using Q-450 system from Dantec Dynamics. To perform measurements, the face of the sample was painted with white mat paint and then a black speckle cover was sprayed (Figure 1) and recorded by one camera during the experiments with a frequency of one shot per second. In order to analyze the obtained results, the field of view in recorded images was divided into a number of facets in the range of 30 to 40 pixels with an experimental resolution of the acquired images of 54 pixels per millimetre, avoiding about one facet from the edges of the samples. The facets were tracked in the speckle pattern during each test for the measurement of sample displacement. The average displacements of the uppermost and lowermost rows of facets as Y-direction displacements and leftmost and rightmost columns of facets as X-direction displacements were used for axial and lateral strain calculations, respectively. In addition to the measurements of

load and displacement, the temperature of the sample was also measured during the experiments by attaching a thermocouple to the backside of the samples with a thermal conductive paste.
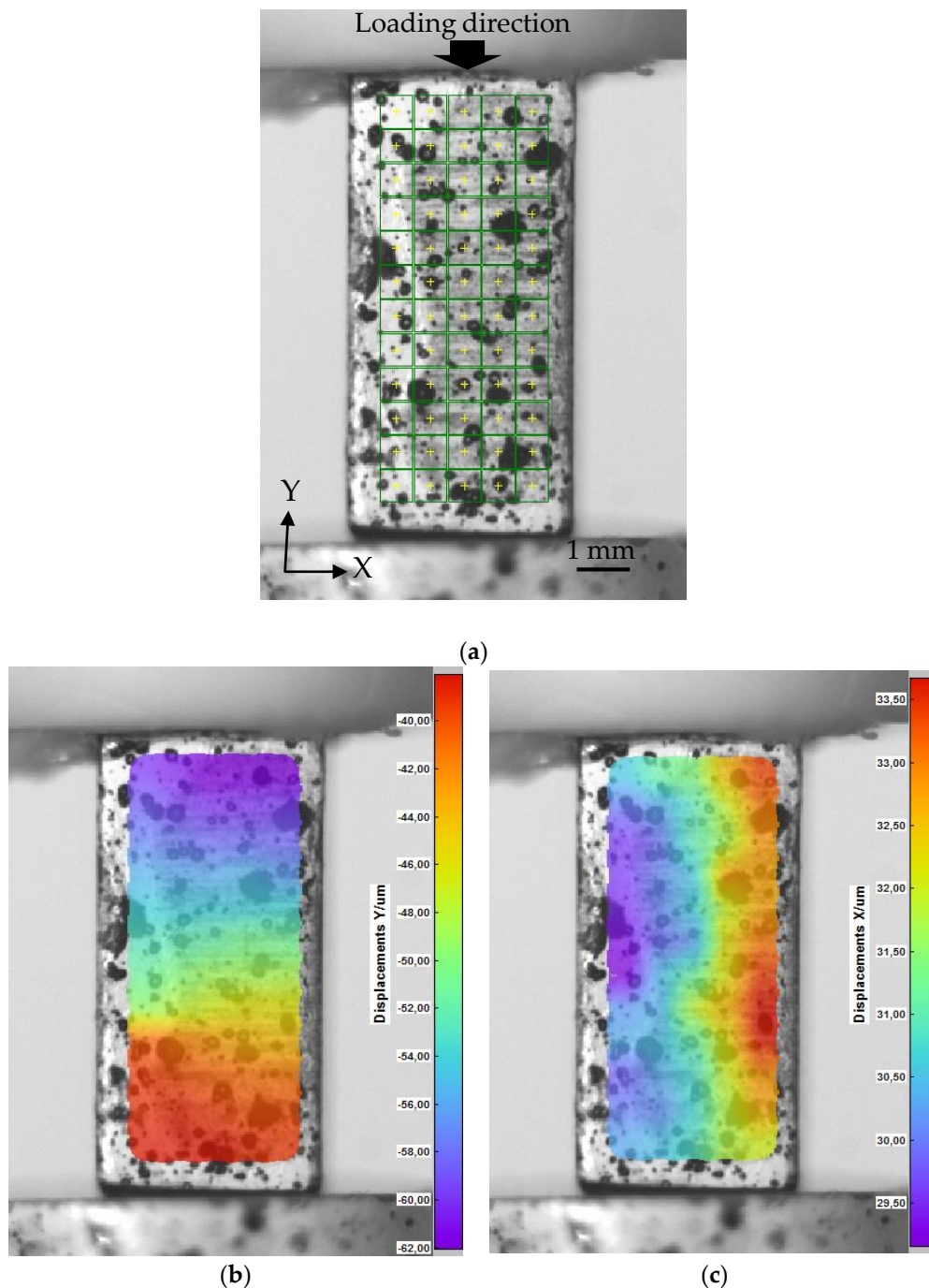

(a)

(b)　　　　　　　　　　　　　　　　　　　　　(c)

Figure 1. (**a**) Evaluated surface of $(La_{0.6}Sr_{0.4})_{0.95}Co_{0.2}Fe_{0.8}O_{3-\delta}$ (LSCF)-P20/50 MPa sample with depicted facets used for the evaluation, (**b**) axial and (**c**) lateral color map displacements at maximum load.

3. Results and Discussion

Figure 2 show the micrographs of annealed bars before the compression tests. As it can be seen in Figure 2a,c, spherical pores with an average diameter of 3.1 ± 0.7 µm are homogenously distributed in samples LSCF-P5 which showed 15% bulk porosity. In comparison, LSCF-P20 samples have a 35% bulk porosity with an interconnected pore structure as shown in Figure 2b,d.
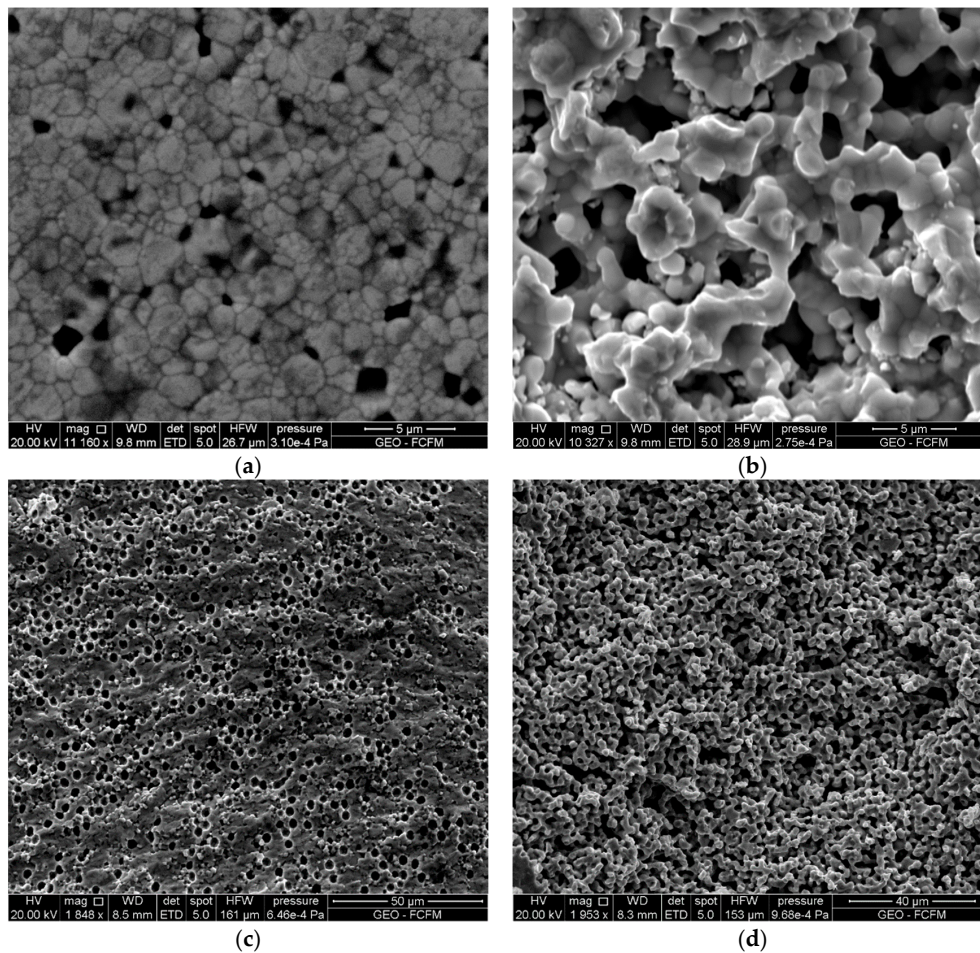
(a)

(b)

(c)

(d)

Figure 2. SEM images of surface of samples (**a**) LSCF-P5 and (**b**) LSCF-P20 after annealing and the fracture surface of samples (**c**) LSCF-P5 and (**d**) LSCF-P20.

The axial and lateral stress–strain curves of LSCF-P5 and LSCF-P20 specimens obtained for two altered maximum loads of 25 and 50 MPa are shown in Figure 3. As it can be seen, the non-linearity of axial and lateral strain–stress curves were detected, which emphasizes the ferroelastic behavior of porous LSCF samples. As summarized in Table 1, the remnant strain increased but the loading moduli and the critical stress decreased with increasing the porosity as reported earlier for LSCF [19,20].
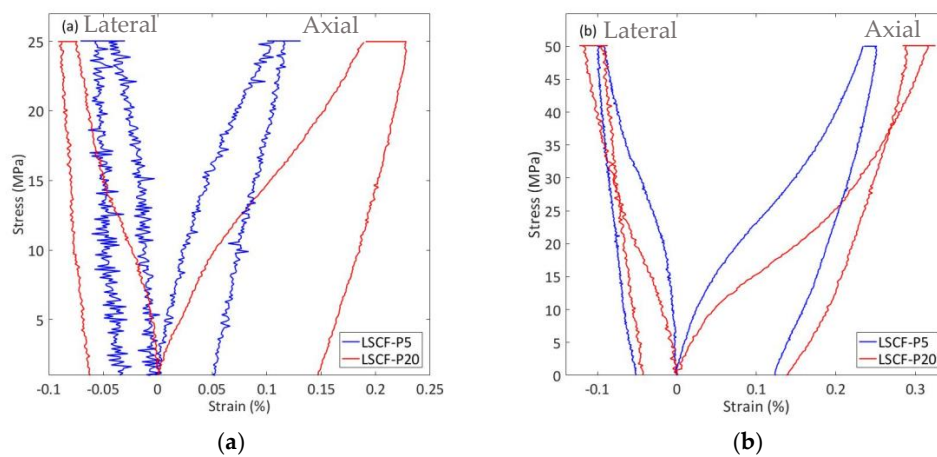

(a)

(b)

Figure 3. Comparison of axial and lateral stress–strain curves of samples with different porosity and maximum stresses of (**a**) 25 MPa and (**b**) 50 MPa.

	PMMA wt %	Porosity (%)	Average Grain Size (μm)	σ_c (MPa)	E_1 (GPa)	E_s (GPa)	E_2 (GPa)	$\Delta\varepsilon_s$ (%)
LSCF-P5	5	15 ± 2	1.6	23	35	14	26	0.04
LSCF-P20	20	35 ± 3	1.7	18	21	9	23	0.11

Figures 4–7 show axial and lateral strains as a function of holding time superimposed with the sample's temperature for samples held for three hours at different constant stresses of 25 and 50 MPa, which show a positive axial and negative lateral creep for LSCF-P5 samples and the LSCF-P20 sample at 25-MPa constant stress. However, the LSCF-P20 sample showed a clear negative axial and positive lateral creep at 50 MPa. As it can be seen, some fluctuations are detected in both axial and lateral creep strain, which coincide with temperature variation of samples due to controlling the temperature of laboratory by air-conditioner so that they can be related to the thermal expansion and contraction of samples with the environment temperature variations. To eliminate the effect of temperature variation, it is considered that total strain (ε_t) is

$$\varepsilon_t = \varepsilon_C(t, \sigma) + \varepsilon_{Th}(T) \tag{1}$$

where ε_{Th} is thermal expansion which assumed to be linear as

$$\varepsilon_{Th} = \alpha.\Delta(T - T_0) \tag{2}$$

where α is the coefficient of thermal expansion of the material at temperature T_0 which is the sample temperature at the start time of holding at maximum stress and ε_c is ferroelastic creep which can be described by a Prony series as

$$\varepsilon_c = \sum c_i \exp\left(\frac{-t}{\tau_i}\right) \tag{3}$$

where c_i and τ_i are constants and t is the holding time. As shown in Figure 8, the deformation of some samples with room temperature variations without applied stress was measured and Equation (2) was used to simulate the obtained strain by which the coefficient of thermal expansion ($\alpha = 50 \times 10^{-6}$ °C^{-1}) was estimated. The obtained coefficient was used to calculate thermal deformation to be extracted from the total strain in all tests as shown in Figures 4–7. The obtained coefficient of thermal expansion is higher than those reported in the literature [21,22], which may be attributed to the temperature range used in this study and further investigation is required to clarify this difference.
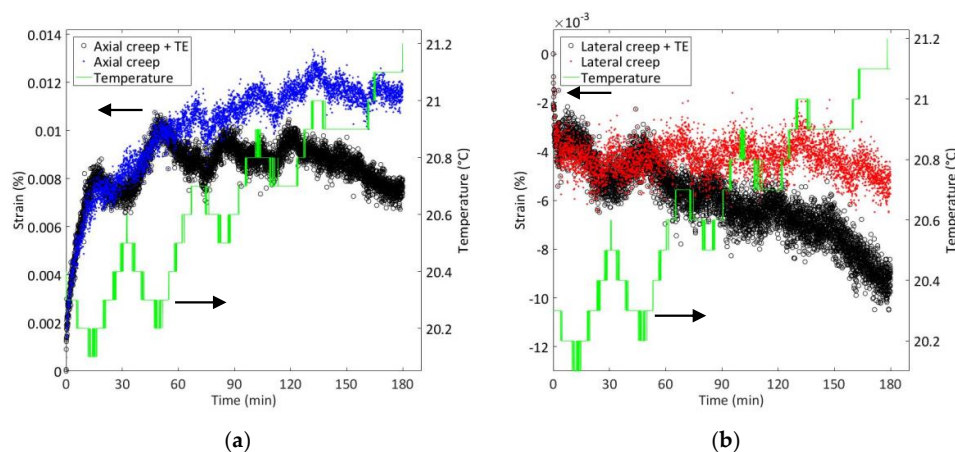

(a) (b)

Figure 4. (**a**) Axial and (**b**) lateral creep deformations of LSCF-P5 sample for 3 h under 25-MPa maximum stress superimposed with a temperature measurement during the experiment.
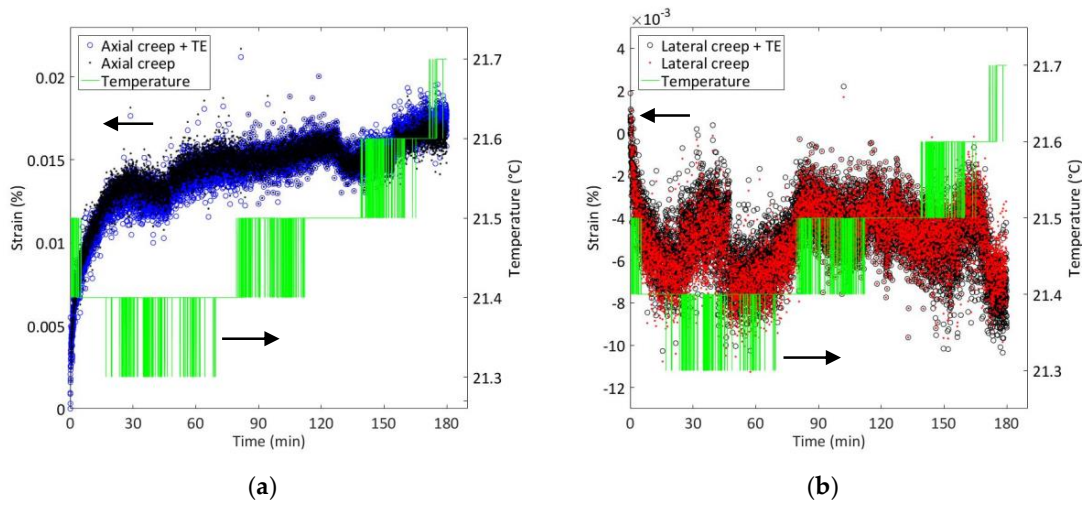
Figure 5. (**a**) Axial and (**b**) lateral creep deformations of LSCF-P5 sample for 3 h under 50-MPa maximum stress superimposed with a temperature measurement during the experiment.
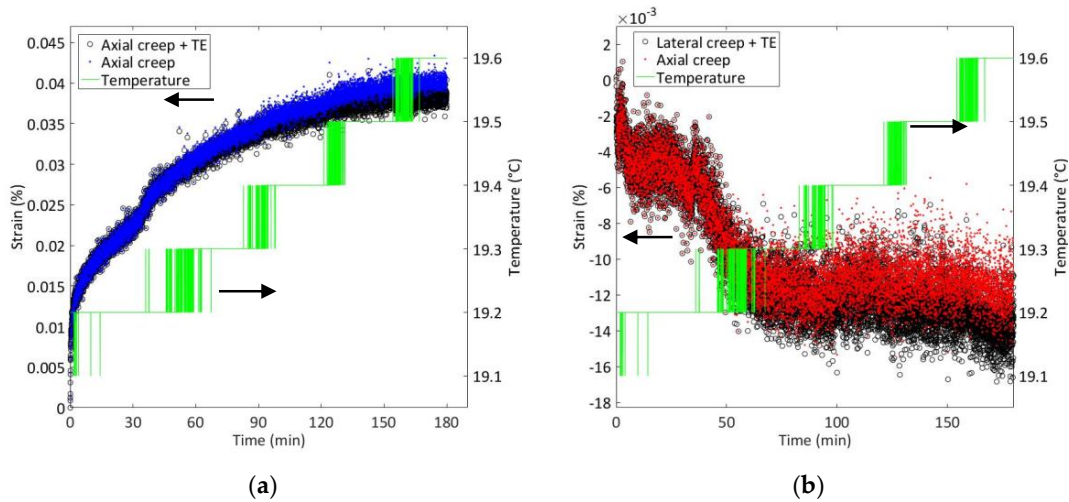

Figure 6. (**a**) Axial and (**b**) lateral creep deformations of LSCF-P20 sample for 3 h under 25-MPa maximum stress superimposed with a temperature measurement during the experiment.
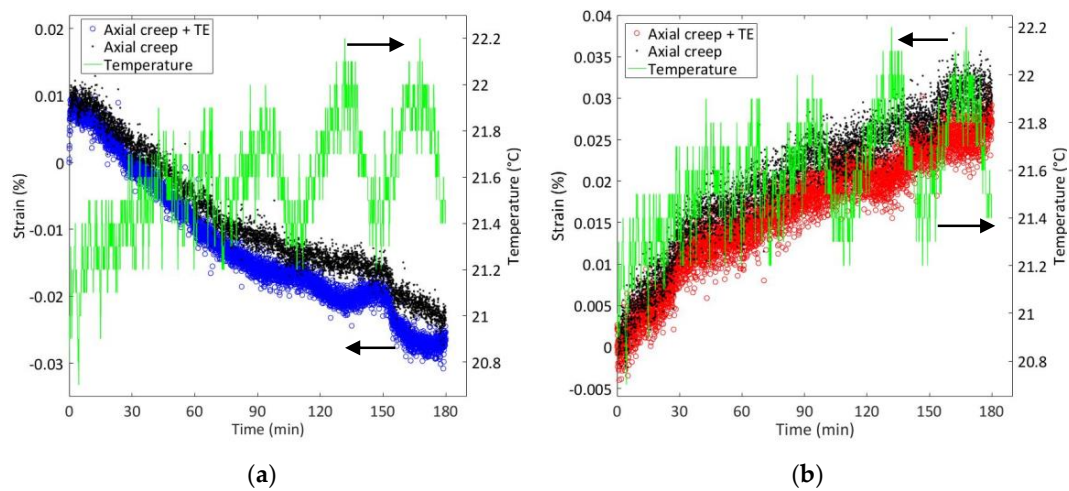

Figure 7. (**a**) Axial and (**b**) lateral creep deformations of LSCF-P20 sample for 3 h under 50-MPa maximum stress superimposed with temperature measurement during the experiment.
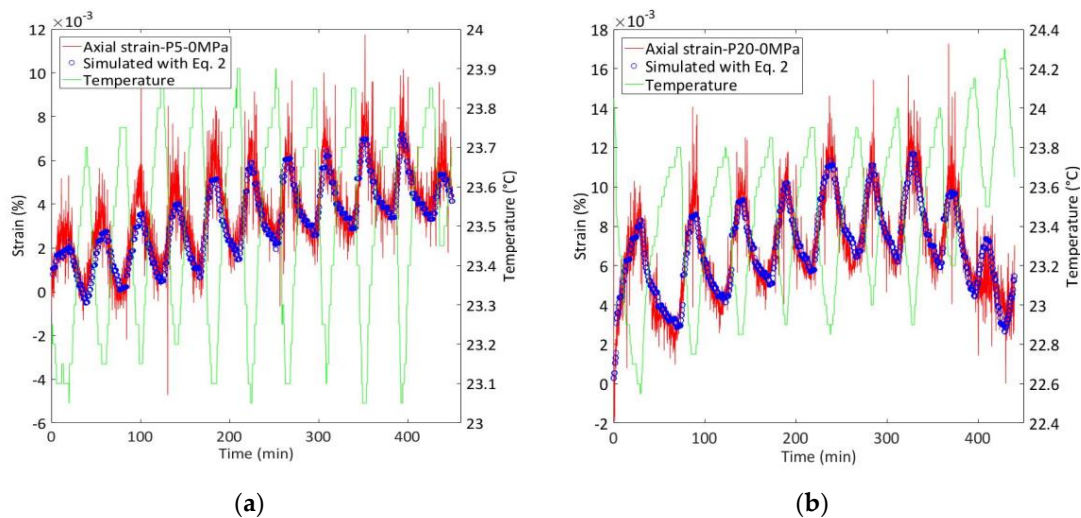
Figure 8. Axial strain deformation of (**a**) LSCF-P5 and (**b**) LSCF-P20 samples without applied compression stress superimposed with a simulated strain and temperature measurement during the experiment.

As it can be seen in Figures 4a, 5a and 6a, the creep deformation of the LSCF-P5 sample at 25 and 50 MPa and P20 at 25 MPa showed a positive axial creep behavior similar to those reported for relatively dense $La_{0.58}Sr_{0.4}Co_{0.2}Fe_{0.8}O_{3-\delta}$ (6% porosity) [3], $LaCoO_3$ [15] and $La_{0.8}Ca_{0.2}CoO_3$ [17] so that they can similarly be described by a Prony series equation as depicted in Figure 9 and Table 2. Additionally, in contrary to the results reported for $LaCoO_3$ [17], the creep rate near critical stress is not higher than those at higher stresses. Figure 7a,b show the axial and lateral creep deformation of sample LSCF-P20 at a maximum stress of 50 MPa, respectively. The axial creep strain shows an increase for about one minute then the sample started to expand axially and contract laterally, which clearly shows negative creep deformation as reported for $LaCoO_3$ [17].

The mechanisms which govern room temperature creep are related to domain switching and domain walls' movement induced by external forces (mechanical stresses, electrical or magnetic fields) and nucleation and growth of new domains into already existing domains [23,24]. By using an in-situ neutron diffraction experiment, Lugovy et al. [17] showed that the movement of the domain walls compelled by the external stress in ferroelastic $LaCoO_3$ perovskite leads to texture formation and there is a variation in the amount of different mobile domains in the sample kept under constant applied stress over time. They discussed forces acting on ferroelastic domain walls and the equation of domain wall mobility suggests the presence of the equilibrium position of these walls at any assumed applied stress. However, they are not able to get the equilibrium positions or even pass these position in practice because of their inertia. Therefore, it creates a situation where the applied stress reaches a value and remains constant, but the domain walls still move forward or backward, which corresponds to the positive or negative or oscillating creep strains. The ferroelastic creep behavior of LSCF is dependent on the rate of the domain nucleation and growth during loading and holding at maximum stress and the porosity enables domain nucleation due to it providing more nucleation sites on free surface of pores [25]; with increasing porosity, critical stress is decreased and a higher creep rate is observed at loads near critical stress and finally negative creep is observed at a higher stress of 50 MPa in samples with higher porosities.
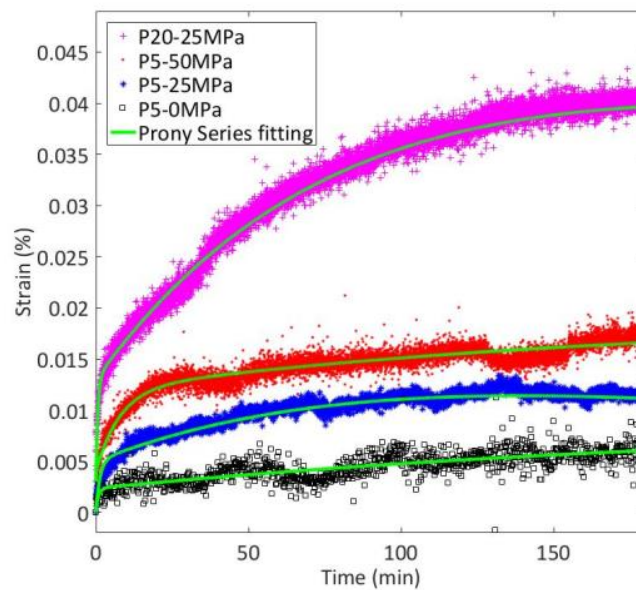
Figure 9. Comparison of axial creep deformation of LSCF-P5 samples under 0, 25 and 50 MPa and LSCF-P20 under 25-MPa maximum load stress and LSCF-P20 sample under 25-MPa maximum stress fitted with Prony series equation.

Table 2. Prony series equation description of axial creep deformations.

	Prony Series Equation	**R²**
LSCF-P5-0MPa	$\varepsilon_c = 0.167 \exp(0.0041t) - 0.004 \exp(-0.584t) - 0.163 \exp(0.003t)$	0.87
LSCF-P5-25MPa	$\varepsilon_c = 0.113 \exp(0.0051t) - 0.005 \exp(-0.764t) - 0.108 \exp(-0.0065t)$	0.94
LSCF-P5-50MPa	$\varepsilon_c = -0.24 \exp(-0.0019t) - 0.008 \exp(-0.129t) + 0.252 \exp(-0.0017t)$	0.89
LSCF-P20-25MPa	$\varepsilon_c = 0.051 \exp(0.00082t) - 0.038 \exp(-0.12t) + 0.013 \exp(-1.636t)$	0.99

4. Conclusions

A digital image correlation technique as a facile and non-contact optical metrology was used for uniaxial compression tests of porous LSCF to study axial and lateral strain–stress curves and ferroelastic creep deformation under two constant stresses of 25 and 50 MPa above critical stress. The results show that stress and porosity are influencing factors not only on strain–stress curves but also on ferroelastic creep deformation so that, with increasing porosity and applied stress, negative creep behavior was observed in LSCF.

Author Contributions: A.A.-F. designed and directed the project and wrote the manuscript. B.A., A.A.-F. and V.M. carried out the experiments. A.A.-F., N.O. and W.A. discussed the results and contributed to the final manuscript. All authors have read and agreed to the published version of the manuscript.

Conflicts of Interest: The authors declare no conflict of interest.

References

1. Akbari-Fakhrabadi, A.; Meruane, V.; Jamshidijam, M.; Garcia-Pinilla, M.A.; Garcia, R.; Orellana, M. Structural and mechanical properties of $La_{0.6}Sr_{0.4}M_{0.1}Fe_{0.9}O_{3-\delta}$ (M: Co, Ni and Cu) perovskites. *Ceram. Int.* **2017**, *43*, 2089–2094. [CrossRef]

2. Li, N.; Boréave, A.; Deloume, J.-P.; Gaillard, F. Catalytic combustion of toluene over a Sr and Fe substituted $LaCoO_3$ perovskite. *Solid State Ion.* **2008**, *179*, 1396–1400. [CrossRef]

3. Araki, W.; Malzbender, J. Ferroelastic deformation of $La_{0.58}Sr_{0.4}Co_{0.2}Fe_{0.8}O_{3-\delta}$ under uniaxial compressive loading. *J. Eur. Ceram. Soc.* **2013**, *33*, 805–812. [CrossRef]

4. Johnsson, M.; Lemmens, P. Crystallography and Chemistry of Perovskites. In *Handbook of Magnetism and Advanced Magnetic Materials*; John Wiley & Sons: Hoboken, NJ, USA, 2007; pp. 1–11.

5. Streiffer, S.K.; Parker, C.B.; Romanov, A.E.; Lefevre, M.; Zhao, L.; Speck, J.S.; Pompe, W.; Foster, C.M.; Bai, G.R. Domain patterns in epitaxial rhombohedral ferroelectric films. I. Geometry and experiments. *J. Appl. Phys.* **1998**, *83*, 2742–2753. [CrossRef]

6. Belenkaya, I.V.; Bragina, O.A.; Nemudry, A.P. Mixed Ionic-Electronic Conducting Perovskites as Nanostructured Ferroelastics. In *Advanced Nanomaterials for Catalysis and Energy*; Elsevier: Amsterdam, The Netherlands, 2019; pp. 515–555.

7. Keitsiro, A. Possible Species of Ferromagnetic, Ferroelectric, and Ferroelastic Crystals. *Phys. Rev. B* **1970**, *2*, 754.

8. Salje, E.K.H. Ferroelastic Materials. *Annu. Rev. Mater. Res.* **2012**, *42*, 265–283. [CrossRef]

9. Orlovskaya, N.; Browning, N.; Nicholls, A. Ferroelasticity in mixed conducting $LaCoO_3$ based perovskites: A ferroelastic phase transition. *Acta Mater.* **2003**, *51*, 5063–5071. [CrossRef]

10. Araki, W.; Takeda, K.; Arai, Y. Mechanical behaviour of ferroelastic lanthanum metal oxides $LaMO_3$ (M = Co, Al, Ga, Fe). *J. Eur. Ceram. Soc.* **2016**, *36*, 4089–4094. [CrossRef]

11. Akbari-Fakhrabadi, A.; Rodríguez, O.; Rojas, R.; Meruane, V.; Pishahang, M.H. Ferroelastic behavior of $LaCoO_3$: A comparison of impression and compression techniques. *J. Eur. Ceram. Soc.* **2019**, *39*, 1569–1576. [CrossRef]

12. Lugovy, M.; Aman, A.; Orlovskaya, N.; Slyunyayev, V.; Graule, T.; Kuebler, J.; Reece, M.J.; Chen, Y.; Ma, N.; An, K. Time and frequency dependent mechanical properties of $LaCoO_3$-based perovskites: Neutron diffraction and domain mobility. *J. Appl. Phys.* **2018**, *124*, 205104. [CrossRef]

13. Zhou, D.; Kamlah, M. Room-temperature creep of soft PZT under static electrical and compressive stress loading. *Acta Mater.* **2006**, *54*, 1389–1396. [CrossRef]

14. Forrester, J.S.; Kisi, E.H. Ferroelastic switching in a soft lead zirconate titanate. *J. Eur. Ceram. Soc.* **2004**, *24*, 595–602. [CrossRef]

15. Araki, W.; Abe, T.; Arai, Y. Ferroelasticity and spin-state transitions of $LaCoO_3$. *J. Appl. Phys.* **2014**, *116*, 043513. [CrossRef]

16. Lugovy, M.; Slyunyayev, V.; Orlovskaya, N.; Verbylo, D.; Reece, M.J. Room-temperature creep of $LaCoO_3$-based perovskites: Equilibrium strain under compression. *Phys. Rev. B* **2008**, *78*, 024107. [CrossRef]

17. Lugovy, M.; Orlovskaya, N.; Pathak, S.; Radovic, M.; Lara-Curzio, E.; Verbylo, D.; Kuebler, J.; Graule, T.; Reece, M.J. Time and frequency dependent mechanical properties of $LaCoO_3$-based perovskites: Internal friction and negative creep. *J. Appl. Phys.* **2018**, *124*, 205103. [CrossRef]

18. Pan, Z.; Huang, S.; Su, Y.; Qiao, M.; Zhang, Q. Strain field measurements over 3000 °C using 3D-Digital image correlation. *Opt. Lasers Eng.* **2020**, *127*, 105942. [CrossRef]

19. Islam, M.; Araki, W.; Arai, Y. Mechanical behavior of ferroelastic porous $La_{0.6}Sr_{0.4}Co_{0.2}Fe_{0.8}O_{3-\delta}$ prepared with different pore formers. *Ceram. Int.* **2017**, *43*, 14989–14995. [CrossRef]

20. Islam, N.; Araki, W.; Arai, Y. Mechanical properties of ferroelastic $La_{0.6}Sr_{0.4}Co_{0.2}Fe_{0.8}O_{3-\delta}$ with various porosities and pore sizes. *J. Mater. Sci.* **2019**, *54*, 5256–5265. [CrossRef]

21. Schulze-Küppers, F.; Baumann, S.; Tietz, F.; Bouwmeester, H.J.M.; Meulenberg, W.A. Towards the fabrication of $La_{0.98-x}Sr_xCo_{0.2}Fe_{0.8}O_{3-\delta}$ perovskite-type oxygen transport membranes. *J. Eur. Ceram. Soc.* **2014**, *34*, 3741–3748. [CrossRef]

22. Brisotto, M.; Cernuschi, F.; Drago, F.; Lenardi, C.; Rosa, P.; Meneghini, C.; Merlini, M.; Rinaldi, C. High temperature stability of $Ba_{0.5}Sr_{0.5}Co_{0.8}Fe_{0.2}O_{3-\delta}$ and $La_{0.6}Sr_{0.4}Co_{1-y}Fe_yO_{3-\delta}$ oxygen separation perovskite membrane. *J. Eur. Ceram. Soc.* **2016**, *36*, 1679–1690. [CrossRef]

23. Hwang, S.C.; Lynch, C.S.; Mcmeeking, R.M. Ferroelectric/ferroelastic interactions and a polarization switching model. *Acta Metall. Mater.* **1995**, *43*, 2073–2084. [CrossRef]

24. Huang, B.X.; Steinbrech, R.W.; Malzbender, J. Direct observation of ferroelastic domain effects in LSCF perovskites. *Solid State Ionics* **2012**, *228*, 32–36. [CrossRef]

25. Lu, G.; Li, S.; Ding, X.; Sun, J.; Salje, E.K.H. Ferroelectric switching in ferroelastic materials with rough surfaces. *Sci. Rep.* **2019**, *9*, 15834. [CrossRef] [PubMed]

Publisher's Note: MDPI stays neutral with regard to jurisdictional claims in published maps and institutional affiliations.